Topological phase transition between $\mathbb{Z}_2$ and second-order topological insulators in a kagome circuit

Yating Yang [1,2] Xingyu Chen [3] Zhenhang Pu [3] Jien Wu,[2,*] Xueqin Huang,[2]
Weiyin Deng [2,3,*] Jiuyang Lu,[2,3,*] and Zhengyou Liu[3,4,*]

[1]*College of Mathematics and Physics, Beijing University of Chemical Technology, Beijing 100029, China*
[2]*School of Physics and Optoelectronics, South China University of Technology, Guangzhou, Guangdong 510640, China*
[3]*Key Laboratory of Artificial Micro- and Nanostructures of Ministry of Education and School of Physics and Technology,
Wuhan University, Wuhan 430072, China*
[4]*Institute for Advanced Studies, Wuhan University, Wuhan 430072, China*

The notion of higher-order topological phases has endowed topological states of matter beyond the first order. In this work, we report the topological phase transition between the conventional $\mathbb{Z}_2$ topological insulator and second-order topological insulator in a kagome circuit. Such a phase transition emerges at the competition between the spin-orbit couplings and nonequivalent nearest-neighbor hoppings without breaking symmetry. The bulk topological invariants, the $\mathbb{Z}_2$ index and spin-polarized bulk polarizations, are calculated to describe the complete phase diagram. The one-dimensional gapless helical edge states of $\mathbb{Z}_2$ topological phase and zero-dimensional corner states of second-order topological phase are observed in the ribbon and finite-size circuit samples, respectively. Our findings in the electric circuits provide an experimental bridge to connect the first-order and higher-order topological phases.

Topological insulators (TIs) [1–4], featured with topological boundary states in the bulk bandgap, have flourished for decades and extended from electronic to classical systems, including optic, acoustic, and circuit systems. In recent years, it has been found that d-dimensional (dD) nth-order TIs host $(d-n)$D topological boundary states [5,6], developing the bulk-boundary correspondence. For the first-order TIs, the dimension of the boundary states is one less than that of the bulk states. For example, the Chern insulators characterized by Chern number with broken time-reversal symmetry have chiral edge states [7–11], while the $\mathbb{Z}_2$ TIs described by $\mathbb{Z}_2$ index possess helical edge states protected by the time-reversal symmetry [12–21]. For the higher-order TIs with lower-dimensional boundary states, zero-dimensional (0D) corner states in two-dimensional (2D) second-order TIs (SOTIs) [22–33], 3D third-order TIs [34–37], and 1D hinge states in 3D SOTI [38–41] are extensively studied. The topological origins of SOTIs include quantized multipole moments [42], Wannier-type [43], and boundary-obstructed topological phase [44]. Recently, orbital interactions are proposed to realize TIs in spinless systems [45]. The TIs are extending to the non-Hermitian [46–48] and non-Abelian [49,50] cases.

Phase transitions are essential for the discovery of new phases of matter. It was previously thought that phase transitions could be uniformly described by Landau's spontaneous symmetry breaking theory. However, the occurrence of topological phases has broken through this understanding. The topological phase transition marks the transformation between two different topological phases without changing symmetry, and is described by the change of the bulk topological invariants. For example, the $\mathbb{Z}_2$ TI with $\mathbb{Z}_2$ index $\nu = 1$ can transit to normal insulator with $\nu = 0$, when tuning the staggered sublattice potential and keeping the symmetries [12]. Interestingly, the TIs of different orders can transit to each other with or without breaking symmetries [51–54]. For instance, a 3D acoustic TI can transit to second-order and third-order TIs with Dirac hierarchy by breaking different boundary symmetries [51,52], and the 2D acoustic TIs can transit to SOTIs without changing symmetry [53,54]. Although plenty of effort has been made on the realizations of the topological phase [55–65], the topological phase transition between the first-order and higher-order TIs is yet to be revealed in electric circuits.

In this work, we realize a 2D kagome circuit to observe the topological phase transition between $\mathbb{Z}_2$ TI and SOTI in the presence of time-reversal symmetry. The kagome circuit is based on the inductor-capacitor network, where the spin-orbit couplings are achieved by next-nearest-neighbor capacitors with braided connections and nonequivalent nearest-neighbor hoppings are realized by capacitors with direct connections. Three distinct phases are found in the kagome circuit, including $\mathbb{Z}_2$ TI, SOTI, and normal insulator. The topological phase transition between $\mathbb{Z}_2$ TI and SOTI can be realized by adjusting the values of capacitors, which is experimentally confirmed in two different circuit samples. One is a ribbon sample in $\mathbb{Z}_2$ TI phase, and the dispersions of 1D gapless helical edge states are observed. The other is a triangle-shaped sample in SOTI phase, and the 0D in-gap corner states are confirmed by the voltage responses at corners and field

*Corresponding authors: wje@scut.edu.cn; dengwy@whu.edu.cn; jylu@whu.edu.cn; zyliu@whu.edu.cn
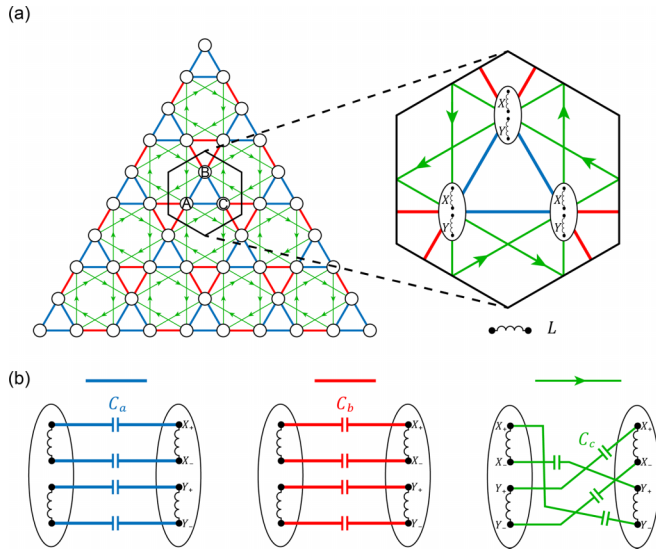
FIG. 1. Schematic of kagome circuit. (a) Kagome circuit with five layers. Nonequivalent nearest-neighbor hoppings are indicated by blue and red lines, spin-orbit couplings are denoted by green lines with arrows. Inset: unit cell marked by black hexagon box. Each site contains two inductances X with nodes $X_\pm$ and Y with nodes $Y_\pm$. (b) Specific circuit connections of capacitors C_a, C_b and C_c, forming the hoppings in (a).

distributions. All the circuit experiments are well consistent with the simulations.

We start from constructing the kagome circuit. Figure 1(a) shows the schematic of kagome circuit with triangle-shaped

geometry, where unit cell (black hexagon box) contains three sites (A, B, and C). Each site is formed by two inductors labeled as X and Y described by the inset at the right panel of Fig. 1(a). Importantly, color lines between sites represent the different hoppings. Red and blue lines between nearest-neighbor sites denote the nonequivalent nearest-neighbor hoppings. Green lines marked with arrows between next-nearest-neighbor sites represent the directional hoppings, which are analogous to the spin-orbit coupling. The circuit realization of these hoppings is illustrated in Fig. 1(b). We make full use of four circuit nodes labeled by $X_\pm$ and $Y_\pm$ at each site to design circuit connections and achieve different hoppings. The nonequivalent nearest-neighbor hoppings can be realized by the direct connections of circuit nodes through capacitor C_a and C_b. The next-nearest-neighbor hoppings are implemented by the braided connections of the circuit nodes through capacitor C_c to construct the spin-orbit coupling. All the inductors have same inductance L.

We then discuss the circuit equations and derive the circuit Hamiltonian to analyze topological properties. According to the Kirchhoff's law and Ohm's law [56], we can obtain the circuit equations for each node in a unit cell as $I = JV$, where I and V are the input current and response potential at these nodes, and circuit Laplacian J is a 12×12 matrix. By the unitary transformation, the circuit Laplacian matrix can be divided into three parts, including spin-up component $J_\uparrow$ with a 3×3 matrix, spin-down component $J_\downarrow$ with a 3×3 matrix, and another component J_0 with a 6×6 matrix possessing trivial solutions. So the topological properties of kagome circuit are only dependent on the spin-up and spin-down components. The spin-up and spin-down voltages are defined as $U_{\uparrow,\downarrow} = U_X \pm iU_Y$, where $U_{X(Y)} = V_{X_+(Y_+)} - V_{X_-(Y_-)}$ is the voltage at
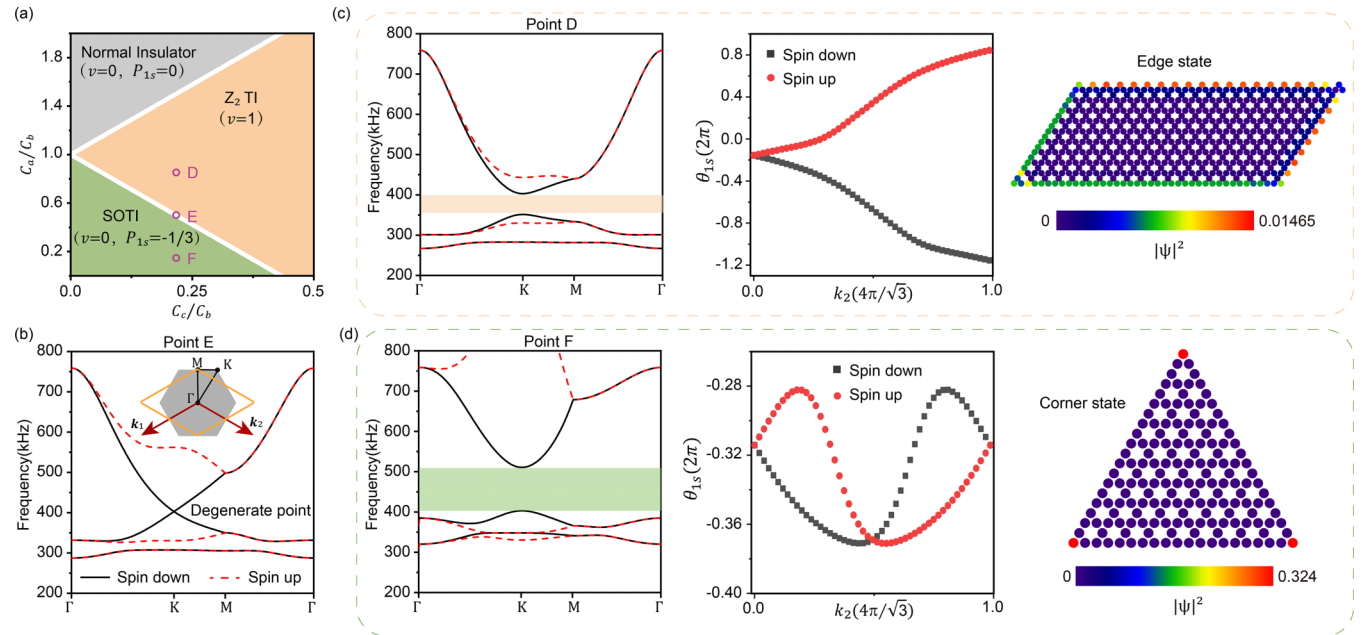
FIG. 2. Phase diagram and typical bulk dispersions of kagome circuits. (a) Phase diagram determined by topological invariants $\mathbb{Z}_2$ index ν and spin-polarized bulk polarization P_{1s}, where $s = \uparrow (\downarrow)$ represents the spin up (spin down). There exist three topologically distinct phases, including $\mathbb{Z}_2$ TI, SOTI, and normal insulator. White lines denote the phase boundaries. (b) Bulk dispersion of point E with a degenerate point. Inset: the first Brillouin zone. (c) and (d) Bulk dispersions with band gaps (left), spin-dependent Wannier bands (middle), and the topological states in band gaps (right) at points D and F, described the $\mathbb{Z}_2$ TI and SOTI, respectively.

the both ends of inductor $X(Y)$. We take the basis vector as $(U_\downarrow^A, U_\downarrow^B, U_\downarrow^C, U_\uparrow^A, U_\uparrow^B, U_\uparrow^C)^T$, and the circuit Hamiltonian

can be deduced by the spin-dependent circuit Laplacian as [66]

$$H = \begin{pmatrix} H_0 - H_{so} & 0 \\ 0 & H_0 + H_{so} \end{pmatrix}, \tag{1}$$

where

$$H_0 = \begin{pmatrix} 0 & C_a + C_b e^{i\mathbf{k}\cdot\mathbf{a}_2} & C_a + C_b e^{i\mathbf{k}\cdot\mathbf{a}_1} \\ C_a + C_b e^{-i\mathbf{k}\cdot\mathbf{a}_2} & 0 & C_a + C_b e^{i\mathbf{k}\cdot\mathbf{a}_3} \\ C_a + C_b e^{-i\mathbf{k}\cdot\mathbf{a}_1} & C_a + C_b e^{-i\mathbf{k}\cdot\mathbf{a}_3} & 0 \end{pmatrix}, \tag{2}$$

$$H_{so} = iC_c \begin{pmatrix} 0 & -e^{-i\mathbf{k}\cdot\mathbf{a}_1} - e^{i\mathbf{k}\cdot\mathbf{a}_3} & e^{i\mathbf{k}\cdot\mathbf{a}_2} + e^{i\mathbf{k}\cdot\mathbf{a}_3} \\ e^{i\mathbf{k}\cdot\mathbf{a}_1} + e^{-i\mathbf{k}\cdot\mathbf{a}_3} & 0 & -e^{i\mathbf{k}\cdot\mathbf{a}_1} - e^{-i\mathbf{k}\cdot\mathbf{a}_2} \\ -e^{-i\mathbf{k}\cdot\mathbf{a}_2} - e^{-i\mathbf{k}\cdot\mathbf{a}_3} & e^{-i\mathbf{k}\cdot\mathbf{a}_1} + e^{i\mathbf{k}\cdot\mathbf{a}_2} & 0 \end{pmatrix}. \tag{3}$$

The lattice constant is set to unity, and $\mathbf{k}$ is the 2D momentum, $\mathbf{a}_1 = (1, 0)$, $\mathbf{a}_2 = (1, \sqrt{3})/2$, and $\mathbf{a}_3 = (1, -\sqrt{3})/2$. H_0 functions as the Hamiltonian of tight-binding kagome lattice, which can possess SOTI phase [43]. H_{so} has the form of the intrinsic spin-orbit coupling, and can lead to the $\mathbb{Z}_2$ TI phase [67]. The Hamiltonian's analysis further verifies that our circuit system can induce the different-order topological phases, offering the possibility of achieving topological phase transition.

The topological invariants are defined to classify topologically distinct phases, including $\mathbb{Z}_2$ index ν to describe the $\mathbb{Z}_2$ TI phase and spin-polarized bulk polarizations P_{1s} (P_{2s}) with $s = \uparrow, \downarrow$ to describe the SOTI phase [66]. Because of the C_3 symmetry, there is $P_{1s} = P_{2s}$. The complete phase diagram determined by ν and P_{1s} is shown in Fig. 2(a), which consists of $\mathbb{Z}_2$ TI ($\nu = 1$) and SOTI ($\nu = 0, P_{1s} = -1/3$) and normal insulator ($\nu = 0, P_{1s} = 0$) phases in the $C_c/C_b - C_a/C_b$ plane. Phase boundaries labeled by white lines are accompanied with the band gap closure, which satisfy $C_a/C_b = \pm 4C_c/(\sqrt{3}C_b) + 1$. For the calculation of phase diagram, there are fixed capacitor $C_b = 10$ nF and inductor $L = 10$ μH. Different phases can be transformed into each other by only adjusting the parameters C_a and C_c without breaking symmetry, hence we can conveniently realize the topological phase transition between different-order topologies.

To investigate the topological phase transition between $\mathbb{Z}_2$ TI and SOTI, we choose three points (D, E, and F) with the same parameter $C_c/C_b = 0.22$. Point D with $C_a/C_b = 0.82$, point E with $C_a/C_b = 0.5$ and point F with $C_a/C_b = 0.1$ are located at $\mathbb{Z}_2$ TI phase, phase boundary, and SOTI phase, respectively. For point E, the spin-up (red dashed lines) and spin-down (black solid lines) frequency dispersions along high symmetry lines of first Brillouin zone are displayed in Fig. 2(b), with a degenerate point representing band gap closure. For point D, the degenerate point is opened to form a $\mathbb{Z}_2$ TI gap, as shown in the left panel of Fig. 2(c). For point F, the degenerate point is opened to form a SOTI gap, as shown in the left panel of Fig. 2(d). As discussed in Ref. [66], the topological properties of kagome circuit can be described by the spin-dependent Wannier bands defined as $\theta_{1s}(k_2) = \int_0^{4\pi/\sqrt{3}} \langle U_s | i\partial k_1 | U_s \rangle dk_1$, where $U_s = U_{\uparrow,\downarrow}$ and $U_\uparrow$

($U_\downarrow$) is the eigenvector for the third spin-up (spin-down) band. The spin Chern numbers can be obtained from the evolution of the spin-dependent Wannier bands as $C_s = \frac{1}{2\pi} \int_{k_2} d\theta_{1s}$. In
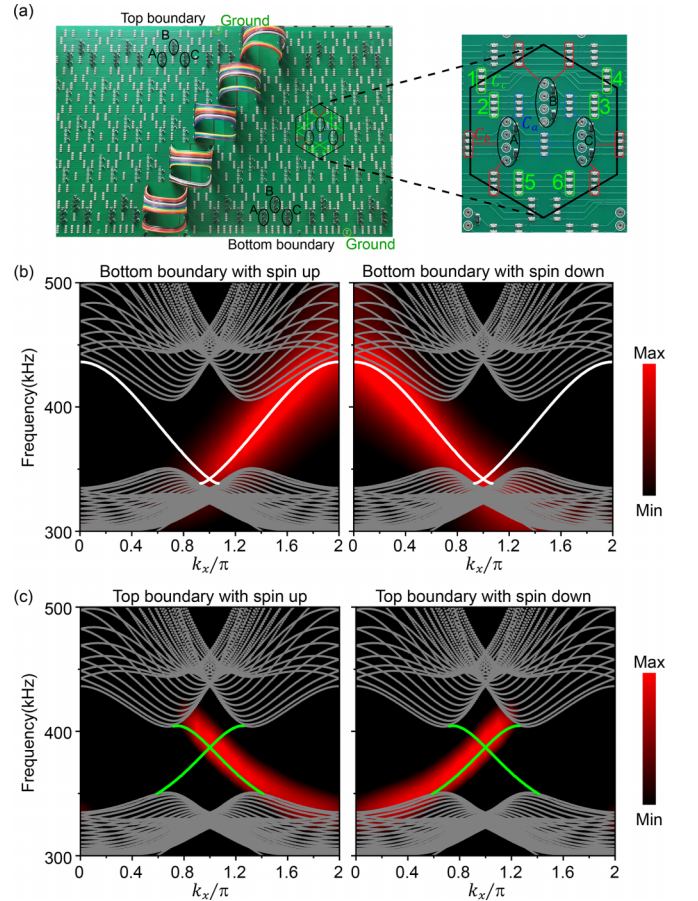
FIG. 3. Observations of 1D gapless helical edge states in $\mathbb{Z}_2$ TI. (a) Partial detail photo of ribbon circuit sample. Enlarged image shows the circuit unit cell, corresponding to the schematic one. (b) and (c) Edge dispersions with spin up (left panel) and spin down (right panel) of bottom and top boundaries. Color maps denote the experimental results, and the gray (white and green) dots denote the numerical bulk (edge) states. The parameters are selected as $C_a = 8.2$ nF, $C_b = 10$ nF, $C_c = 2.2$ nF, and $L = 10$ μH.
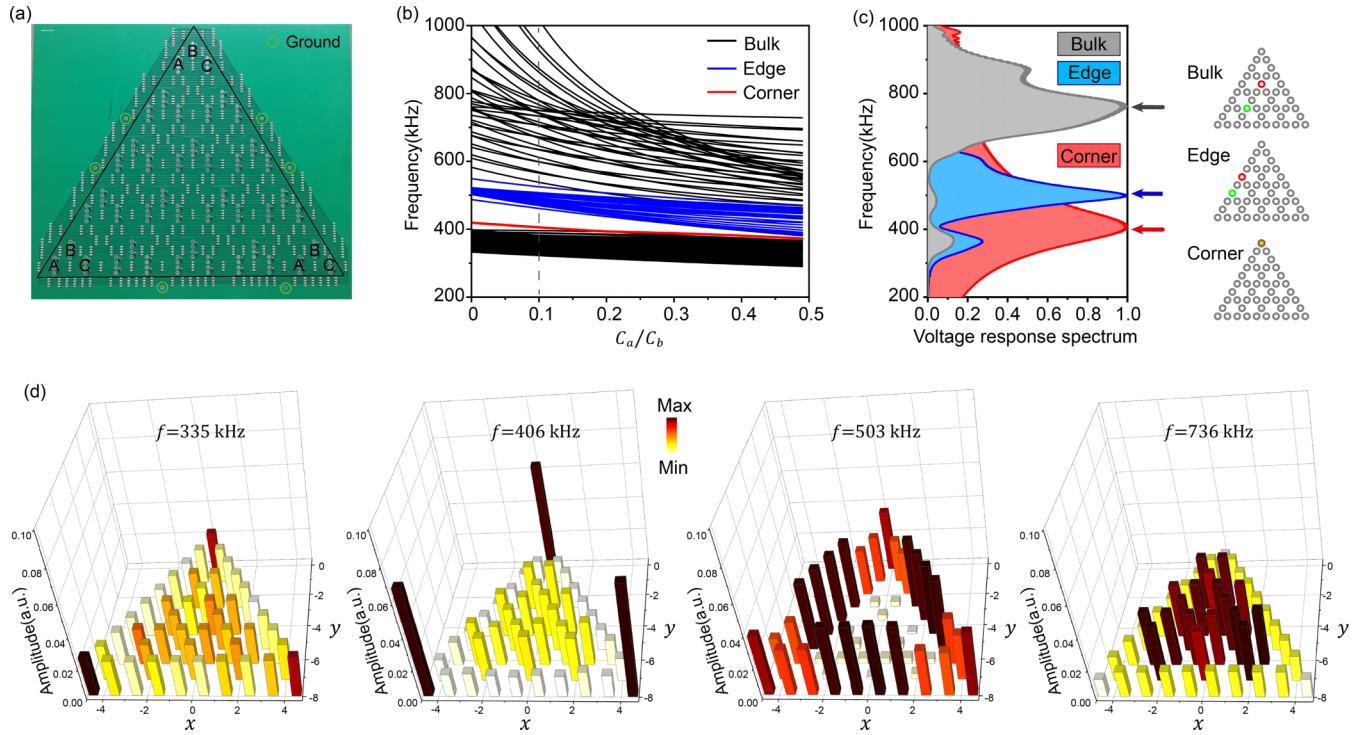
FIG. 4. Observations of 0D corner states in SOTI. (a) Photo of triangle-shaped circuit sample with five layers. (b) Frequency spectra as a function of C_a/C_b, included bulk, corner and edge modes. (c) Left panel: measured bulk, edge and corner voltage response spectra. Right panel: red (green) circle marks the position of the source (detector). (d) Measured spin-up voltage field distributions at different frequencies, corresponding to bulk, corner, edge and bulk modes, respectively. The color denotes the normalized magnitude. The parameters are chosen as $C_a = 1$ nF, $C_b = 10$ nF, $C_c = 2.2$ nF, and $L = 10$ μH.

the middle panel of Fig. 2(c), θ_{1s} varies ± 1 along k_2, showing the spin Chern numbers $C_s = \pm 1$ and leading to $\mathbb{Z}_2$ TI with $v = (C_\uparrow - C_\downarrow)/2 = 1$. In the middle panel of Fig. 2(d), θ_{1s} vary 0 along k_2, resulting to $v = 0$. And the spin-polarized bulk polarizations can be defined as $P_{1s} = \frac{-1}{S_{BZ}} \int_0^{4\pi/\sqrt{3}} \theta_{1s} dk_2$ where S_{BZ} is the area of the first Brillouin zone [68], which are equal to the exact values of $-1/3$, revealing the SOTI phase. By calculating the finite structures, we can get the topological states in the bandgaps: edge state and corner state, as shown in the right panels of Figs. 2(c) and 2(d), respectively. Consequently, by reducing C_a, the $\mathbb{Z}_2$ TI gap with edge states is closed to a degenerate point, and then reopen as a SOTI gap with corner states, realizing the topological phase transition between different-order topologies.

According to the bulk-boundary correspondence, the $\mathbb{Z}_2$ TI phase with $v = 1$ supports the existence of 1D gapless helical edge states. Here, we investigate the edge states based on a ribbon circuit sample with period boundary condition along the x direction and open boundary condition along the y direction. To obtain $\mathbb{Z}_2$ TI phase, the parameters are chosen as those of point D in the phase diagram, where $C_a/C_b = 0.82$, $C_c/C_b = 0.22$, $C_b = 10$ nF and $L = 10$ μH. The ribbon circuit is experimentally implemented by a finite sample with 21×5 unit cells, as depicted in Fig. 3(a). The enlarged image of circuit unit cell shows the one-to-one correspondence with the model shown in Fig. 1. Due to the missing hoppings at boundary sites, it is noted that we set the corresponding capacitors C_a, C_b or C_c to link the ground to compensate for the difference of on-site potentials at these sites.

We observe the dispersions of 1D gapless helical edge states. We first investigate the edge states at bottom boundary, and place a voltage source at node X_+ located at the middle position of bottom boundary. Voltage responses $(U_{X,Y})$ of all the inductor at bottom boundary are measured. By the Fourier transforming $U_\uparrow = U_X + iU_Y$ and $U_\downarrow = U_X - iU_Y$, we can obtain the measured projected dispersions (color map) of spin up and spin down, as shown in the left and right panels of Fig. 3(b), respectively. The calculated projected dispersions of ribbon are revealed by solid curves, in which the white curves represent the gapless helical edge states at bottom boundary, and the gray curves denote the bulk states. One can see that the spin-up and spin-down edge states have the opposite group velocities and transmission directions, forming a pair of helical edge states. In addition, the measured (color map) and calculated (green lines) projected dispersions for edge states at top boundary show in Fig. 3(c), where the voltage source is placed at the top boundary. All the measured results are consistent well with the theories, demonstrating the existence of gapless edge states. By combining Figs. 3(b) and 3(c), a pair of helical edge states transmits oppositely along the bottom (top) boundary, revealing that this kagome circuit is a $\mathbb{Z}_2$ TI.

The SOTI phase with quantized P_{1s} guarantees the existence of 0D corner states in the band gap. We construct a triangle-shaped circuit sample with five layers and 15 unit cells, as shown in Fig. 4(a). The parameters are chosen as $C_c/C_b = 0.22$, $C_b = 10$ nF, and $L = 10$ μH, taking C_a/C_b from 0 to 0.49. According to the phase diagram, the circuit

sample with these parameters has the SOTI phase, and thus possesses corner states. To demonstrate that, we calculate the frequency spectra of triangle-shaped circuit as a function of C_a/C_b, as shown in Fig. 4(b). It is found that the corner states (red lines) emerge from the band gap as expected. In addition, the gapped edge states (blue lines) also appear in the band gap same as the other SOTIs.

Corner states are observed by measuring the voltage responses and voltage field distributions. Here, one case with $C_a/C_b = 0.1$ (point F in the phase diagram) is selected to experimentally demonstrate the existence of corner states. As shown in the left panel of Fig. 4(c), we measure the voltage response spectra of bulk (gray), boundary (blue), and corner (red) of circuit sample. The voltage source is excited at the red site (node X_+) and the voltage response $U_\uparrow$ are recorded at green site, as illustrated in the right panel of Fig. 4(c). One can see that the resonance peaks of corner are observed at 406 kHz, which corresponds to the corner states. Resonance peaks of boundary and bulk result from the edge and bulk states. Corner states can be visualized by measuring the spatial distribution of voltage. Figure 4(d) shows the field distributions of spin-up voltages ($|U_\uparrow|^2$) at the frequencies of lower bulk (335 kHz), corner (406 kHz), edge (503 kHz), and upper bulk (736 kHz) states, and each of them is normalized by the sum of $|U_\uparrow|^2$ at all sites. Results show that the voltages at 406 kHz are well confined at three corners, which is different from the voltages at other frequencies, evidencing the presence of corner states. For the measurements of field distributions, we place a voltage source at node X_+ for one site, and measure the voltage response $U_\uparrow$ at the same site.

In conclusion, we have illustrated a topological phase transition between $\mathbb{Z}_2$ TI and SOTI without breaking symmetry in a kagome circuit. The topological properties of these two different-order topological phases, including 1D helical edge states of the $\mathbb{Z}_2$ TI phase and 0D corner states of the SOTI phase, are demonstrated in circuit simulations and experiments. Our findings may enable the potential applications for the multifunctional topological devices in circuit systems. Our circuit system provides an experimental platform to explore topological phases with multiple orders, which also may be extended to the photonic and elastic wave systems with same or different lattices. Furthermore, it is interesting to unveil the conversions between different-order topological phases in 3D systems, and from this inspire an applicable and adjustable topological circuit.

[1] A. Bansil, H. Lin, and T. Das, *Colloquium:* Topological band theory, Rev. Mod. Phys. **88**, 021004 (2016).

[2] C.-K. Chiu, J. C. Y. Teo, A. P. Schnyder, and S. Ryu, Classification of topological quantum matter with symmetries, Rev. Mod. Phys. **88**, 035005 (2016).

[3] M. Z. Hasan and C. L. Kane, *Colloquium:* Topological insulators, Rev. Mod. Phys. **82**, 3045 (2010).

[4] X.-L. Qi and S.-C. Zhang, Topological insulators and superconductors, Rev. Mod. Phys. **83**, 1057 (2011).

[5] F. Schindler, A. M. Cook, M. G. Vergniory, Z. Wang, S. S. P. Parkin, B. A. Bernevig, and T. Neupert, Higher-order topological insulators, Sci. Adv. **4**, eaat0346 (2018).

[6] B. Xie, H.-X. Wang, X. Zhang, P. Zhan, J.-H. Jiang, M. Lu, and Y. Chen, Higher-order band topology, Nat. Rev. Phys. **3**, 520 (2021).

[7] Z. Wang, Y. Chong, J. D. Joannopoulos, and M. Soljačić, Observation of unidirectional backscattering-immune topological electromagnetic states, Nature (London) **461**, 772 (2009).

[8] G.-G. Liu, Z. Gao, Q. Wang, X. Xi, Y.-H. Hu, M. Wang, C. Liu, X. Lin, L. Deng, S. A. Yang, P. Zhou, Y. Yang, Y. Chong, and B. Zhang, Topological Chern vectors in three-dimensional photonic crystals, Nature (London) **609**, 925 (2022).

[9] Y. Ding, Y. Peng, Y. Zhu, X. Fan, J. Yang, B. Liang, X. Zhu, X. Wan, and J. Cheng, Experimental demonstration of acoustic Chern insulators, Phys. Rev. Lett. **122**, 014302 (2019).

[10] T. Hofmann, T. Helbig, C. H. Lee, M. Greiter, and R. Thomale, Chiral voltage propagation and calibration in a topolectrical Chern circuit, Phys. Rev. Lett. **122**, 247702 (2019).

[11] Z. Wang, Y. Biao, X.-T. Zeng, X. Chen, X.-L. Sheng, S. A. Yang, and R. Yu, Realization in circuits of a Chern state with an arbitrary Chern number, Phys. Rev. B **107**, L201101 (2023).

[12] C. L. Kane and E. J. Mele, Z_2 topological order and the quantum spin Hall effect, Phys. Rev. Lett. **95**, 146802 (2005).

[13] B. A. Bernevig, T. L. Hughes, and S.-C. Zhang, Quantum spin Hall effect and topological phase transition in HgTe quantum wells, Science **314**, 1757 (2006).

[14] E. Prodan, Robustness of the spin-Chern number, Phys. Rev. B **80**, 125327 (2009).

[15] Y. Yang, Z. Xu, L. Sheng, B. Wang, D. Y. Xing, and D. N. Sheng, Time-reversal-symmetry-broken quantum spin Hall effect, Phys. Rev. Lett. **107**, 066602 (2011).

[16] P. Bampoulis, C. Castenmiller, D. J. Klaassen, J. v. Mil, Y. Liu, C.-C. Liu, Y. Yao, M. Ezawa, A. N. Rudenko, and H. J. W. Zandvliet, Quantum spin Hall states and topological phase transition in germanene, Phys. Rev. Lett. **130**, 196401 (2023).

[17] Y. Yang, Z. Gao, H. Xue, L. Zhang, M. He, Z. Yang, R. Singh, Y. Chong, B. Zhang, and H. Chen, Realization of a three-dimensional photonic topological insulator, Nature (London) **565**, 622 (2019).

[18] M. Kim, Z. Wang, Y. Yang, H. T. Teo, J. Rho, and B. Zhang, Three-dimensional photonic topological insulator without spin-orbit coupling, Nat. Commun. **13**, 3499 (2022).

[19] C. He, X. Ni, H. Ge, X.-C. Sun, Y.-B. Chen, M.-H. Lu, X.-P. Liu, and Y.-F. Chen, Acoustic topological insulator and robust one-way sound transport, Nat. Phys. **12**, 1124 (2016).

[20] W. Deng, X. Huang, J. Lu, V. Peri, F. Li, S. D. Huber, and Z. Liu, Acoustic spin-Chern insulator induced by synthetic spin-orbit coupling with spin conservation breaking, Nat. Commun. **11**, 3227 (2020).

[21] Y. T. Yang, D. J. Zhu, Z. H. Hang, and Y. D. Chong, Observation of antichiral edge states in a circuit lattice, Sci. China-Phys. Mech. Astron. **64**, 257011 (2021).

[22] B.-Y. Xie, G.-X. Su, H.-F. Wang, H. Su, X.-P. Shen, P. Zhan, M.-H. Lu, Z.-L. Wang, and Y.-F. Chen, Visualization of higher-order topological insulating phases in two-dimensional dielectric photonic crystals, Phys. Rev. Lett. **122**, 233903 (2019).

[23] L. He, Z. Addison, E. J. Mele, and B. Zhen, Quadrupole topological photonic crystals, Nat. Commun. **11**, 3119 (2020).

[24] Y. Qi, C. Qiu, M. Xiao, H. He, M. Ke, and Z. Liu, Acoustic realization of quadrupole topological insulators, Phys. Rev. Lett. **124**, 206601 (2020).

[25] H. Xue, Y. Yang, F. Gao, Y. Chong, and B. Zhang, Acoustic higher-order topological insulator on a kagome lattice, Nat. Mater. **18**, 108 (2019).

[26] X. Ni, M. Weiner, A. Alù, and A. B. Khanikaev, Observation of higher-order topological acoustic states protected by generalized chiral symmetry, Nat. Mater. **18**, 113 (2019).

[27] X. Zhang, H. X. Wang, Z. K. Lin, Y. Tian, B. Xie, M. H. Lu, Y. F. Chen, and J. H. Jiang, Second-order topology and multidimensional topological transitions in sonic crystals, Nat. Phys. **15**, 582 (2019).

[28] S. Imhof, C. Berger, F. Bayer, J. Brehm, L. W. Molenkamp, T. Kiessling, F. Schindler, C. H. Lee, M. Greiter, T. Neupert, and R. Thomale, Topolectrical-circuit realization of topological corner modes, Nat. Phys. **14**, 925 (2018).

[29] J. Wu, X. Huang, J. Lu, Y. Wu, W. Deng, F. Li, and Z. Liu, Observation of corner states in second-order topological electric circuits, Phys. Rev. B **102**, 104109 (2020).

[30] M. Ezawa, Edge-corner correspondence: Boundary-obstructed topological phases with chiral symmetry, Phys. Rev. B **102**, 121405(R) (2020).

[31] Y. Ren, Z. Qiao, and Q. Niu, Engineering corner states from two-dimensional topological insulators, Phys. Rev. Lett. **124**, 166804 (2020).

[32] C. Chen, Z. Song, J.-Z. Zhao, Z. Chen, Z.-M. Yu, X.-L. Sheng, and S. A. Yang, Universal approach to magnetic second-order topological insulator, Phys. Rev. Lett. **125**, 056402 (2020).

[33] X. Huang, J. Lu, Z. Yan, M. Yan, W. Deng, G. Chen, and Z. Liu, Acoustic higher-order topology derived from first-order with built-in Zeeman-like fields, Sci. Bull. **67**, 488 (2022).

[34] X. Zhang, B.-Y. Xie, H.-F. Wang, X. Xu, Y. Tian, J.-H. Jiang, M.-H. Lu, and Y.-F. Chen, Dimensional hierarchy of higher-order topology in three-dimensional sonic crystals, Nat. Commun. **10**, 5331 (2019).

[35] H. Xue, Y. Ge, H.-X. Sun, Q. Wang, D. Jia, Y.-J. Guan, S.-Q. Yuan, Y. Chong, and B. Zhang, Observation of an acoustic octupole topological insulator, Nat. Commun. **11**, 2442 (2020).

[36] X. Ni, M. Li, M. Weiner, A. Alù, and A. B. Khanikaev, Demonstration of a quantized acoustic octupole topological insulator, Nat. Commun. **11**, 2108 (2020).

[37] S. Liu, S. Ma, Q. Zhang, L. Zhang, C. Yang, O. You, W. Gao, Y. Xiang, T. J. Cui, and S. Zhang, Octupole corner state in a three-dimensional topological circuit, Light Sci. Appl. **9**, 145 (2020).

[38] C. Yue, Y. Xu, Z. Song, H. Weng, Y.-M. Lu, C. Fang, and X. Dai, Symmetry-enforced chiral hinge states and surface quantum anomalous Hall effect in the magnetic axion insulator $Bi_{2-x}Sm_xSe_3$, Nat. Phys. **15**, 577 (2019).

[39] Q. Wei, X. Zhang, W. Deng, J. Lu, X. Huang, M. Yan, G. Chen, Z. Liu, and S. Jia, 3D hinge transport in acoustic higher-order topological insulators, Phys. Rev. Lett. **127**, 255501 (2021).

[40] C. He, H.-S. Lai, B. He, S.-Y. Yu, X. Xu, M.-H. Lu, and Y.-F. Chen, Acoustic analogues of three-dimensional topological insulators, Nat. Commun. **11**, 2318 (2020).

[41] J. Du, T. Li, X. Fan, Q. Zhang, and C. Qiu, Acoustic realization of surface-obstructed topological insulators, Phys. Rev. Lett. **128**, 224301 (2022).

[42] W. A. Benalcazar, B. A. Bernevig, and T. L. Hughes, Quantized electric multipole insulators, Science **357**, 61 (2017).

[43] M. Ezawa, Higher-order topological insulators and semimetals on the breathing kagome and pyrochlore lattices, Phys. Rev. Lett. **120**, 026801 (2018).

[44] E. Khalaf, W. A. Benalcazar, T. L. Hughes, and R. Queiroz, Boundary-obstructed topological phases, Phys. Rev. Res. **3**, 013239 (2021).

[45] F. Gao, X. Xiang, Y. G. Peng, X. Ni, Q. L. Sun, S. Yves, X. F. Zhu, and A. Alu, Orbital topological edge states and phase transitions in one-dimensional acoustic resonator chains, Nat. Commun. **14**, 8162 (2023).

[46] K. Ding, C. Fang, and G. Ma, Non-Hermitian topology and exceptional-point geometries, Nat. Rev. Phys. **4**, 745 (2022).

[47] Q. Zhou, J. Wu, Z. Pu, J. Lu, X. Huang, W. Deng, M. Ke, and Z. Liu, Observation of geometry-dependent skin effect in non-Hermitian phononic crystals with exceptional points, Nat. Commun. **14**, 4569 (2023).

[48] B. Liu, Y. Li, B. Yang, X. Shen, Y. Yang, Z. H. Hang, and M. Ezawa, Experimental observation of non-Hermitian higher-order skin interface states in topological electric circuits, Phys. Rev. Res. **5**, 043034 (2023).

[49] Q. Guo, T. Jiang, R.-Y. Zhang, L. Zhang, Z.-Q. Zhang, B. Yang, S. Zhang, and C. T. Chan, Experimental observation of non-Abelian topological charges and edge states, Nature (London) **594**, 195 (2021).

[50] J. Wu, Z. Wang, Y. Biao, F. Fei, S. Zhang, Z. Yin, Y. Hu, Z. Song, T. Wu, F. Song, and R. Yu, Non-Abelian gauge fields in circuit systems, Nat. Electron. **5**, 635 (2022).

[51] L.-Y. Zheng and J. Christensen, Dirac hierarchy in acoustic topological insulators, Phys. Rev. Lett. **127**, 156401 (2021).

[52] L. Yang, Y. Wang, Y. Meng, Z. Zhu, X. Xi, B. Yan, S. Lin, J. Chen, B. Shi, Y. Ge, S. Yuan, H. Chen, H. Sun, G.-G. Liu, Y. Yang, and Z. Gao, Observation of Dirac hierarchy in three-dimensional acoustic topological insulators, Phys. Rev. Lett. **129**, 125502 (2022).

[53] Y. Yang, H. Sun, J. Lu, X. Huang, W. Deng, and Z. Liu, Variable-order topological insulators, Commun. Phys. **6**, 143 (2023).

[54] X.-C. Sun, H. Chen, H.-S. Lai, C.-H. Xia, C. He, and Y.-F. Chen, Ideal acoustic quantum spin Hall phase in a multi-topology platform, Nat. Commun. **14**, 952 (2023).

[55] V. V. Albert, L. I. Glazman, and L. Jiang, Topological properties of linear circuit lattices, Phys. Rev. Lett. **114**, 173902 (2015).

[56] J. Ningyuan, C. Owens, A. Sommer, D. Schuster, and J. Simon, Time- and site-resolved dynamics in a topological circuit, Phys. Rev. X **5**, 021031 (2015).

[57] C. H. Lee, S. Imhof, C. Berger, F. Bayer, J. Brehm, L. W. Molenkamp, T. Kiessling, and R. Thomale, Topolectrical Circuits, Commun. Phys. **1**, 39 (2018).

[58] Y. Li, Y. Sun, W. Zhu, Z. Guo, J. Jiang, T. Kariyado, H. Chen, and X. Hu, Topological LC-circuits based on microstrips and observation of electromagnetic modes with orbital angular momentum, Nat. Commun. **9**, 4598 (2018).

[59] W. Zhu, S. Hou, Y. Long, H. Chen, and J. Ren, Simulating quantum spin Hall effect in the topological Lieb lattice of a linear circuit network, Phys. Rev. B **97**, 075310 (2018).

[60] M. Ezawa, Electric circuits for non-Hermitian Chern insulators, Phys. Rev. B **100**, 081401(R) (2019).

[61] W. Zhu, Y. Long, H. Chen, and J. Ren, Quantum valley Hall effects and spin-valley locking in topological Kane-Mele circuit networks, Phys. Rev. B **99**, 115410 (2019).

[62] M. Ezawa, Higher-order topological electric circuits and topological corner resonance on the breathing kagome and pyrochlore lattices, Phys. Rev. B **98**, 201402(R) (2018).

[63] J. Wu, X. Huang, Y. Yang, W. Deng, J. Lu, W. Deng, and Z. Liu, Non-Hermitian second-order topology induced by resistances in electric circuits, Phys. Rev. B **105**, 195127 (2022).

[64] K. Luo, R. Yu, and H. Weng, Topological nodal states in circuit lattice, Research **2018**, 6793752 (2018).

[65] W. Zhang, D. Zou, Q. Pei, W. He, J. Bao, H. Sun, and X. Zhang, Experimental observation of higher-order topological Anderson insulators, Phys. Rev. Lett. **126**, 146802 (2021).

[66] See Supplemental Material at http://link.aps.org/supplemental/10.1103/PhysRevB.109.165406 for (I) Circuit Laplacian, (II) Bloch Hamiltonian, and (III) Calculations of topological invariants, (IV) The presence of global loss.

[67] H.-M. Guo and M. Franz, Topological insulator on the kagome lattice, Phys. Rev. B **80**, 113102 (2009).

[68] H.-X. Wang, G.-Y. Guo, and J.-H. Jiang, Band topology in classical waves: Wilson-loop approach to topological numbers and fragile topology, New J. Phys. **21**, 093029 (2019).